Surface-wave array tomography in SE Tibet from ambient seismic noise and two-station analysis – I. Phase velocity maps

Huajian Yao,[1] Robert D. van der Hilst[1] and Maarten V. de Hoop[2]

[1]*Department of Earth, Atmospheric, and Planetary Sciences, Massachusetts Institute of Technology, Cambridge, MA, 02139, USA. E-mail: hjyao@mit.edu*
[2]*Center for Computational and Applied Mathematics, Purdue University, West Lafayette, IN, 47907, USA*

GJI Seismology

SUMMARY
Empirical Green's functions (EGFs) between pairs of seismographs can be estimated from the time derivative of the long-time cross-correlation of ambient seismic noise. These EGFs reveal velocity dispersion at relatively short periods, which can be used to resolve structures in the crust and uppermost mantle better than with traditional surface-wave tomography. We combine Rayleigh-wave dispersion estimates from EGFs and from traditional two-station (TS) analysis into a new approach to surface-wave array tomography with data from dense receiver arrays. We illustrate the methodology with continuous broad-band recordings from a temporary seismographic network on the southeastern part of the Tibetan plateau, in Sichuan and Yunnan provinces, SW China. The EGFs are robust under temporal changes in regional seismicity and the use of either ambient noise (approximated by records without signal from events with magnitude $m_b \geq 5$ or 4) or surface wave coda produces similar results. The EGFs do not strongly depend on the presence of large earthquakes, but they are not reciprocal for stations aligned in the N–S direction. This directionality reflects the paucity of seismicity to the north of the array. Using a far-field representation of the surface-wave Green's function and an image transformation technique, we infer from the EGFs the Rayleigh-wave phase velocity dispersion in the period band from 10–30 s. A classical TS approach is used to determine Rayleigh-wave phase velocity dispersion between 20–120 s. Together, they constrain phase velocity variations for $T = 10$–120 s, which can be used to study the structure from the crust to the upper mantle. Beneath SE Tibet, short and intermediate period (10–80 s) phase velocities are prominently low, suggesting that the crust and upper mantle beneath SE Tibet is characterized by slow shear wave propagation.

Key words: array tomography, empirical Green's functions, phase velocity, SE Tibet, surface waves, two-station method.

1 INTRODUCTION

Surface-wave tomography based on ballistic waves propagating from a source to multiple receivers has provided important information about the 3-D shear wave velocity structure in the upper mantle both on a global (Trampert & Woodhouse 1996; Shapiro & Ritzwoller 2002, to name but a few) and regional (e.g. Zielhuis & Nolet 1994; Simons *et al.* 2002; Huang *et al.* 2003) scale. In these studies, depth resolution is obtained from (fundamental and/or higher mode) group or phase velocity dispersion, with the low-frequency component constraining deeper structures than the high-frequency ones. Accurate imaging of the shallow part of the lithosphere, including the crust, is of particular interest for understanding the relationships between mantle dynamics and geologic processes at or near the surface. Unfortunately, if one considers surface-wave dispersion along source–receiver paths, the resolution of structure in the relevant depth range is often limited by: (1) scattering at the short-period part ($T < 30$ s) of the waveforms; (2) inadequate path

coverage due to the uneven distribution of seismic sources and receivers; (3) insufficient information about the seismic source; and (4) uncertainties about the spatial characteristics of the surface-wave sensitivity kernel (e.g. Spetzler *et al.* 2002; Yoshizawa & Kennett 2002; Zhou *et al.* 2004).

Recent studies show that surface-wave Green's function between two seismograph stations can be estimated from the long-time cross-correlation of coda waves (Campillo & Paul 2003) and ambient seismic noise (Shapiro & Campillo 2004; Shapiro *et al.* 2005; Sabra *et al.* 2005a). The surface-wave periods considered in these studies are shorter than those that can (reliably) be used in traditional analyses of source–receiver propagation. Moreover, measurements can, in principle, be made for any pair of receivers within seismograph arrays, and the dense path coverage thus produced enables high-resolution surface-wave tomography (Shapiro *et al.* 2005; Sabra *et al.* 2005b). Previous studies used group velocity dispersion extracted from the noise cross-correlation function (Shapiro & Campillo 2004; Shapiro *et al.* 2005)—hereinafter referred to as

NCF—or from its time derivative, the empirical Green's function (Sabra *et al.* 2005a,b)—hereinafter EGF. Theoretically, the time derivative of the NCF is equivalent to the Green's function except for a frequency-dependent amplitude factor (Lobkis & Weaver 2001; Weaver & Lobkis 2004; Roux *et al.* 2005), but in contrast to the real Green's functions, which are by definition reciprocal and independent of the seismic source, the EGFs that are estimated from actual coda waves or ambient seismic noise may be time asymmetrical due to the inhomogeneous distribution of noise sources and attenuation (Paul *et al.* 2005; Sabra *et al.* 2005a).

Group dispersion measurements rely on amplitude information and may, therefore, be affected by distortion of the amplitude spectrum of the EGF. The phase information in EGFs estimated from the NCF is, however, theoretically the same as that of the real Green's function. In this paper we demonstrate that accurate phase velocity dispersion measurements can be obtained from the EGF by using the far-field representation of the surface-wave Green's function and an image transformation technique.

Traditional global and regional surface-wave tomography relies on relatively long period data and assumes integration over wave paths—or finite frequency kernels—between source and receivers that are often many thousands of kilometres apart. Such approaches cannot fully exploit the potential data redundancy (and resulting spatial resolution) provided by dense receiver arrays. In principle, better spatial localization can be obtained with the classical two-station (TS) method (Knopoff *et al.* 1966), which measures phase-velocity dispersion between two stations in the intermediate and longer periods range using cross-correlation. For example, Passier *et al.* (1997) use the TS approach to SKIPPY array data in Australia. Brisbourne & Stuart (1998) invert shear wave velocity structure beneath North Island, New Zealand, from Rayleigh-wave interstation phase velocities. Recently, Yao *et al.* (2005) introduce an image transformation technique to measure interstation phase velocity dispersion and presented Rayleigh-wave phase velocity maps from 15 to 120 s in western China and adjacent regions.

Here we explore how the Rayleigh-wave phase velocity dispersion data from the Green's function and the TS methods can be integrated into a method for high-resolution surface-wave array tomography of continental lithosphere. We show applications to data from a temporary array of 25 broad-band seismometers operated by MIT and CIGMR (Chengdu Institute of Geology and Mineral Resources) on the southeastern Tibetan plateau, in Sichuan and Yunnan provinces, SW China (Fig. 1). We carry out the analysis up to the construction of phase velocity maps for surface-wave periods of 10–120 s. The inversion for and interpretation of shear heterogeneity in the crust and upper mantle beneath the study region will presented elsewhere (Yao, Beghein, Van der Hilst, in preparation, 2006).

2 EMPIRICAL GREEN'S FUNCTION (EGF)

We calculate EGFs from continuous vertical component seismograms recorded from 2004 April to July. The instrument response has been removed from all the data prior to cross-correlation. We conduct several experiments to test the robustness of the EGFs for temporal variations and directionality of the 'noise' signals. First, we compare EGFs calculated for different time periods. Second, we compare the EGFs reconstructed from data in different frequency bands and discuss the effects of the spatial distribution of the 'noise' sources. Third, we calculate EGFs from ambient seismic 'noise' using records in which signal from known earthquakes (considering
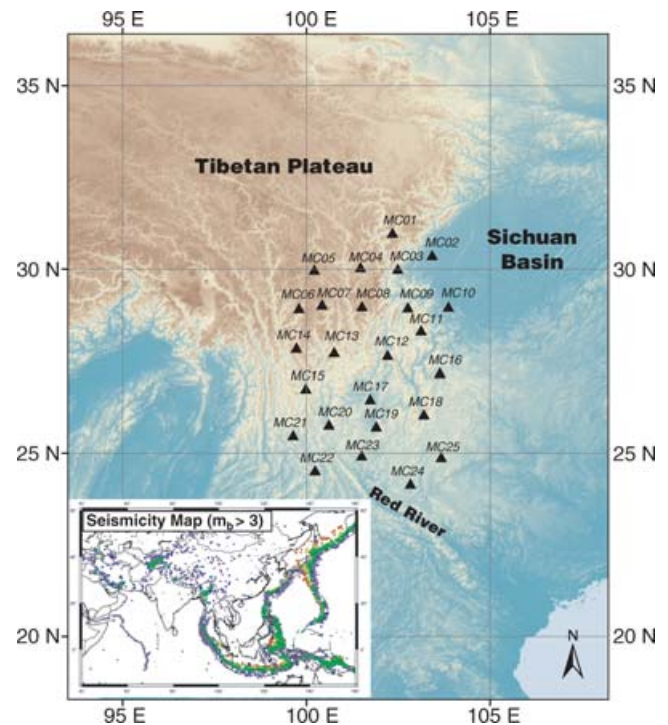
Figure 1. The location of 25 stations of the MIT–CIGMR array. The inset (lower left): epicenter of earthquakes with $m_b > 3$ that occurred in 2004 (Engdahl *et al.* 1998).

different magnitude cut-offs) is suppressed. Fourth, for comparison, we also calculate EGFs explicitly from the surface-wave coda. In this paper we use the term 'noise' rather loosely either for scattered waves or for the parts of the records that are not directly related to (known) large events. In the latter case, 'noise' may contain signal from background seismicity, not just microseismic activity.

2.1 Noise correlation

Previous studies (Lobkis & Weaver 2001; Weaver & Lobkis 2004; Roux *et al.* 2005; Sabra *et al.* 2005a) have demonstrated that EGFs obtained from the noise cross-correlation function (NCF), by taking the time derivative, are equivalent to real Green's function except for a frequency-dependent amplitude correction. For hypothetical seismograph stations at position A and B, the relationship between the NCF, $C(t)$, the EGF, $\hat{G}(t)$, and the real (unknown) Green's function, $G(t)$, can be represented as

$$\frac{dC_{AB}(t)}{dt} = -\hat{G}_{AB}(t) + \hat{G}_{BA}(-t) \approx -G_{AB}(t) + G_{BA}(-t). \quad (1)$$

Here, the approximation indicates that the EGF, $\hat{G}(t)$, may differ from the exact Green's function, $G(t)$, because of effects of anelasticity and specific spatial distribution and spectral properties of the (ambient) noise (Roux *et al.* 2005; Paul *et al.* 2005). Later in this section we will illustrate some of these effects, but for notational simplicity we will drop the distinction of $\hat{G}$ and G. In eq. (1), $G_{AB}(t)$ is the actual Green's function at receiver B for a fictitious (point) source located at A, and $G_{BA}(-t)$ is the time-reversed Green's function at A for a fictitious (point) source at B. In view of causality, $G_{AB}(t)$ contributes at $t \geq 0$ and $G_{BA}(-t)$ contributes at $t \leq 0$. Furthermore, $C_{AB}(t)$ is the approximate cross-correlation function between

the two stations given by

$$C_{AB}(t) \approx \int_0^{t_C} v_A(\tau)v_B(t+\tau)\,d\tau, \qquad (2)$$

where $v_A(t)$ and $v_B(t)$ are the continuously recorded, but time-windowed broad-band data at stations A and B, respectively, and t_C is the total cross-correlation time (i.e. observation time).

The $\pi/2$ phase shift between EGF and NCF does not influence estimates of the group velocity between points A and B: indeed, some studies use NCFs (Shapiro & Campillo 2004; Shapiro *et al.* 2005), whereas others prefer to use EGFs because the time deriva-tion enhances the higher frequencies (Sabra *et al.* 2005a,b). The change in amplitude spectrum may, however, affect the group ve-locity measurements. In contrast, phase velocities do not depend on the amplitude information, but ignoring the phase shift produces an error, which becomes significant if the interstation distance AB is comparable to or less than the wavelengths considered. In this study, we compute the phase velocities from the EGFs.

2.2 Temporal variations from microseisms and scatter

To test the robustness of the EGFs we compute them for different time periods: for this purpose, we arbitrarily choose the months of 2004 April, May, June, and July. In a first set of experiments, we use a (generous) group-velocity window (2–10 km s^{-1}) to mute the wave trains from earthquakes with $m_b \geq 6$ (that is, in the correspond-ing group-velocity window we set the amplitude to zero) in order to approximate cross-correlations from ambient 'noise' (which in-cludes signal that is not directly related to large events). We follow Campillo & Paul (2003) and Shapiro & Campillo (2004) to compute for every possible station pair the NCF by one-bit cross-correlation of the vertical component seismograms which are both band-pass filtered in the period bands 10–60 s. We do this for each month sepa-rately. The time t in eq. (2) is from $-t_m$ to t_m; $t_m = \Delta/v_m$, with Δ the interstation distance and v_m the minimum group velocity, which is set to be 1.5 km s^{-1}. Figs 2(a) and 3 show, for different station pairs, that the EGFs constructed from recordings in the different months are similar to one another.

2.3 Directionality and amplitude spectrum

Theoretically, the Green's functions $G_{AB}(t)$ and $G_{BA}(-t)$ should be each others reciprocal. However, EGFs may become one sided due to preferred directions to noise sources, for example, the ocean micro-seisms in the study by Sabra *et al.* (2005a). For our study, Figs 2(a), 3(a), (c) and (d) reveal a clear directionality: the EGFs for station pairs lining up in N–S direction are one sided whereas the sta-tions lining up in E–W direction are much more symmetric (e.g. Fig. 3b).

In order to investigate if this difference depends on frequency, for station pair MC04-MC23 we compute EGFs in different period bands (10–20, 20–30, 30–40, and 40–60 s) (Fig. 4). In the period bands 10–20 s (Fig. 4a) and 20–30 s (Fig. 4b) the EGFs are one sided and stable over the 4 months. However, in the period bands 30–40 s (Fig. 4c) and 40–60 s (Fig. 4d) the EGFs do not show the one-sided feature and the different months yield different re-sults. Similar frequency dependencies are observed for other station pairs.

The EGFs in the period bands 10–20 s (Fig. 4a) are very similar to those for 10–60 s (Fig. 2a). Amplitude spectra, shown in Fig. 5 for April, reveal that the dominant frequency band of the EGFs is
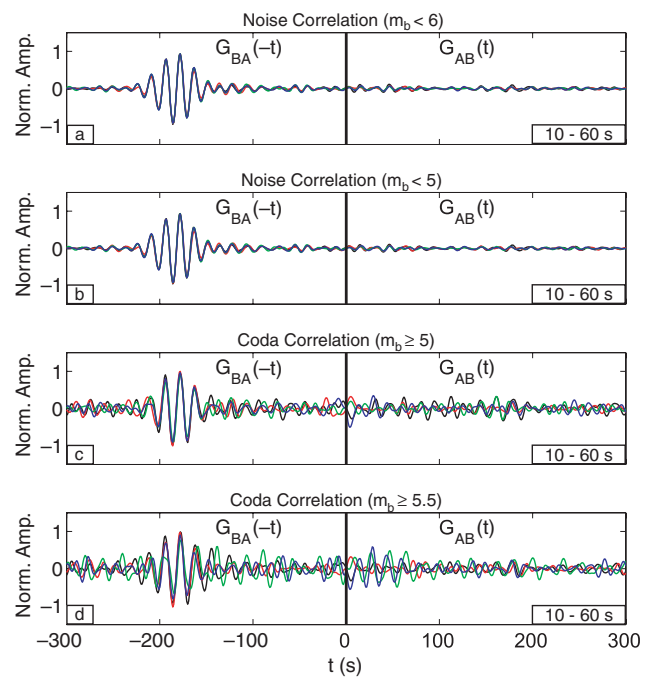

Figure 2. EGFs in the period bands 10–60 s from one-bit cross-correlation of vertical component ambient seismic noise (a, b) and surface-wave coda (c, d) of the two-station pair MC04-MC23 for 4 months in 2004 (black—April, red—May, green—June and blue—July). The right half ($t > 0$) and the left half ($t < 0$) of each plot represent the EGF from MC04 (source) to MC23 (receiver) and the EGF from MC23 to MC04, respectively. For (a), using a group-velocity window, wave trains from earthquakes with $m_b \geq 6.0$ are muted for both stations before the cross-correlation, and the same for (b) but with $m_b \geq 5.0$. For (c) only surface-wave code from earthquakes with $m_b \geq 5.0$ are kept for the cross-correlation and the same for (d) but with $m_b \geq 5.5$. 'Norm. Amp.' on the vertical axis means 'normalized amplitude'.
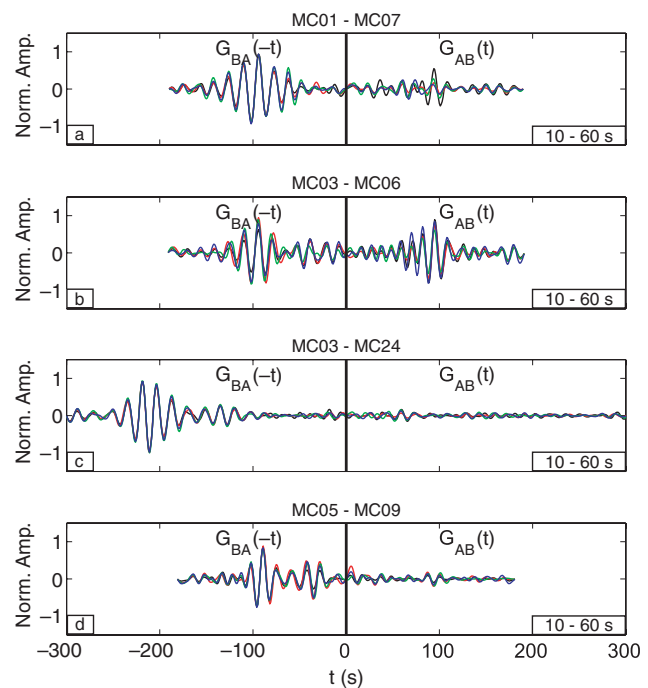

Figure 3. EGFs (normalized amplitude) from the cross-correlation of am-bient seismic noise of different station pairs in the period bands 10–60 s for 4 months in 2004 as in Fig. 2(a).
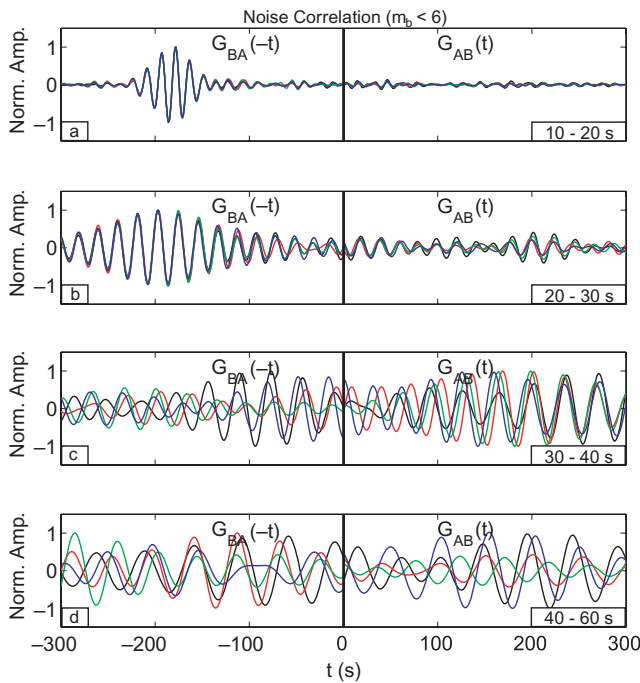
Figure 4. EGFs (normalized amplitude) from the cross-correlation of ambient seismic noise of the two-station pair MC04-MC23 for 4 months in 2004 as in Fig. 2(a) but in different period bands: (a) 10–20 s; (b) 20–30 s; (c) 30–40 s; and (d) 40–60 s.
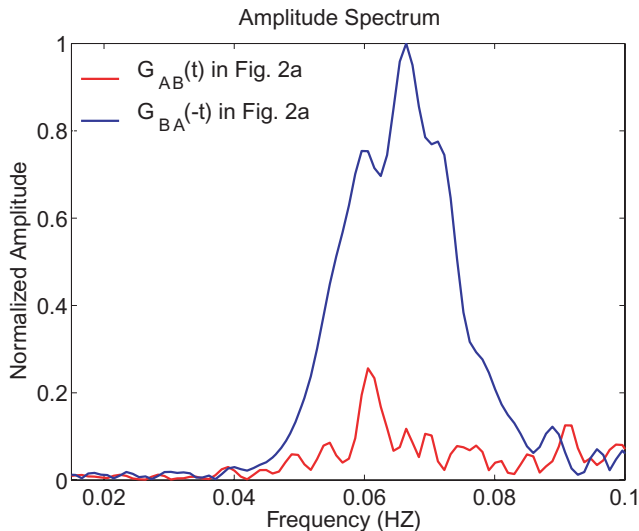

Figure 5. Amplitude spectrum of the EGF of the two-station pair MC04-MC23 for 2004 April (black waveform in Fig. 2a): blue line for the left part of the EGF and red line for the right part of the EGF.

~0.08–0.05 Hz (i.e. ~12–20 s) and that their energy is very low at frequencies less than 0.04 Hz (or periods larger than 25 s). The latter may explain the instability of the EGFs observed in Figs 4(c) and (d); the low-frequency waves do not create coherent waves between the station pair. It seems reasonable to assume that the one-sided feature (that is, the failure of reciprocity) in EGFs for the N–S direction is primarily due to the significant lack of seismicity north of the array (Fig. 1, inset), in combination with interstation scattering. However, it is not obvious why the expression of this is so different in the intermediate or longer period bands ($T > 30$ s), and the part of the

data that contributes to the EGFs at periods larger than 30 s should be investigated further.

2.4 Effects on EGFs of specific earthquakes and noise signals

By definition, a Green's function represents the solution due to a point source and is unrelated to the actual source. This is not, generally, true for EGFs. Indeed, because uneven regional distribution of background seismicity can produce directionality of the EGFs (see above), we should investigate if the presence of large earthquakes can produce bias. For that purpose, we compute EGFs, for $T = 10$–60 s, after muting signal related to (known) earthquakes with $m_b \geq 5$ (instead of the $m_b \geq 6$ used in the experiment described above). The results, shown (again) for station pair MC04-MC23 (Fig. 2b), are almost the same as for input data void only of the signal due to larger earthquakes (Fig. 2a). Tests with magnitude cut-off at 4 or 3 give similar results, which implies that the effect on EGFs from specific earthquakes is small compared to the contributions from microseismicity and ambient noise.

2.5 EGFs from surface-wave coda

It has been demonstrated that the diffusive character of coda waves due to multiple scattering in the lithosphere can be used to estimate the Green's functions between two seismic stations (Campillo & Paul 2003; Paul *et al.* 2005). Therefore, complementary to calculating EGFs from background seismic noise (approximated by the muting of signal from large earthquakes), we calculate them (again with one-bit cross-correlation) from the coda of the surface waves due to large earthquakes. For this purpose we mute much of the data and only keep the surface-wave coda (in the group velocity window 1.5–3 km s^{-1}) from larger earthquakes with $m_b \geq 5$. The EGFs estimated from the surface-wave coda (Fig. 2c) are almost the same (in the surface-wave part) as the EGFs from ambient seismic noise (previous section), but they become increasingly unstable when the magnitude cut-off increases and when, as a consequence, the number of data decreases (Fig. 2d). Similar to the EGFs from ambient seismic noise (Figs 2a and b), the EGFs from coda correlation (Fig. 2c, d) also show time asymmetry due to the predominant directions in the source distribution (Paul *et al.* 2005).

3 PHASE VELOCITY DISPERSION FROM EGFS

Previous studies estimated group velocity dispersion from NCFs (Shapiro & Campillo 2004; Shapiro *et al.* 2005) or EGFs (Sabra *et al.* 2005a,b). Here we demonstrate that phase velocity dispersion can be calculated from the EGF through the use of a far-field representation of the surface-wave Green's function and an image transformation technique (Yao *et al.* 2005). In the far field, the time harmonic wave of the Green's function for the surface-wave fundamental mode at frequency ω is given by (Dahlen & Tromp 1998)

$$\text{Re}\{G_{AB}(\omega) \exp(-i\omega t)\} \approx (8\pi k S)^{-1/2} \cos\left(k_{AB}\Delta - \omega t + \frac{\pi}{4}\right),$$

(3)

where $k_{AB} = \frac{1}{\Delta} \int_0^\Delta k d\Delta = \frac{\omega}{c_{AB}}$ is the average wavenumber between 'source' A and receiver B, c_{AB} is the average phase velocity, Δ is the surface distance traversed by the arrival under consideration between 'source' A and receiver B, S is the geometrical spreading

for surface waves such that $S \rightarrow \sin(\Delta/R)$ (R is the radius of the Earth) towards the source, and $\frac{\pi}{4}$ is remnant of the asymptotic expansion of the Legendre function. We require Δ to be at least three wavelengths (λ) in order to satisfy the far-field approximation. When the phase traveltime t satisfies

$$k_{AB}\Delta - \omega t + \frac{\pi}{4} = 0; \tag{4}$$

it will correspond to one peak in the harmonic wave of Green's function. At that point the average phase velocity c_{AB} at frequency ω can be calculated by

$$c_{AB}(T) = \frac{\Delta}{t - T/8}, \tag{5}$$

where $T = 2\pi/\omega$ is the corresponding period. With the far-field limitation, we require

$$c_{AB} \cdot T = \lambda \leq \Delta/3. \tag{6}$$

For each station pair, eq. (6) determines the largest period to be considered; effectively it produces denser path coverage at shorter periods than at longer periods. For multiresolution imaging this has the attractive property that path coverage will be densest for the shortest period waves considered.

We now illustrate how to extract the phase velocity dispersion curve from the EGF using the far-field approximation and an image transformation technique. First, we band-pass filter the EGFs at central periods from 10 to 60 s, with 1 s intervals and a pass-band width of 0.4 s. (We remark that for non-symmetric correlation functions the side with the larger amplitude is used as the EGF for subsequent analyses—for example, the left side of Fig. 2a.) Then, we construct a time-period $(t - T)$ image (e.g. Fig. 6a) for the surface-wave part (determined by a group-velocity window, for example, 2.5–5 km s^{-1}). Each column of the $t - T$ image represents an amplitude normalized EGF filtered at certain period T (the black trace in Fig. 6(a) is for $T = 20$ s). On the $t - T$ image the frequency dependence is readily observed; notice, for instance, the increase of the phase traveltime with decreasing period (Fig. 6a).

Each column of the $t - T$ image (e.g. the black trace in Fig. 6a) is then transformed to a velocity-coordinate waveform (black trace in Fig. 6b) using eq. (5) and a spline interpolation in order to get an evenly spaced velocity coordinate and to keep the amplitude information unchanged upon transformation. Thus, a peak point at the filtered EGF (e.g. P in Fig. 6a) will have the same phase velocity as that of the corresponding peak at the transformed waveform (e.g. P^* in Fig. 6b). We use this procedure to transform the $t - T$ image to a velocity-period $(c - T)$ image (Fig. 6b). On the $c - T$ image the dispersion curve can be easily identified and automatically picked, and the 2π ambiguity in phase velocity measurement is well resolved. This image transformation technique, introduced by Yao *et al.* (2005) to measure phase velocities for the TS method,
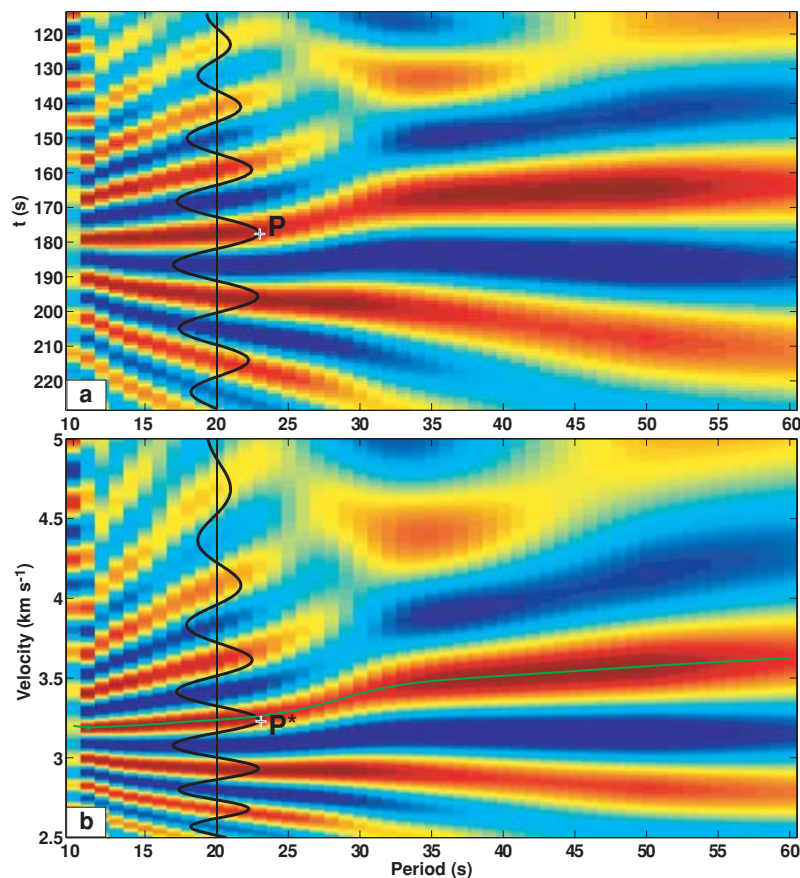
Figure 6. Phase velocity dispersion measurements from the EGF of MC23-MC04 in 2004 April: (a) time-period $(t - T)$ image by narrow band-pass filtering the EGF; the black waveform is the normalized EGF filtered at the central period $T = 20$ s, which corresponds to the column at the $T = 20$ s on the $t - T$ image; (b) velocity-period $(c - T)$ image and phase velocity dispersion measurements (solid green line); the black waveform, which corresponds to the column at the $T = 20$ s on the $c - T$ image, is the transformed velocity coordinate waveform from the waveform in (a) using eq. (5) and a spline interpolation. Red and blue on (a) and (b) represent the peak and trough of the wave trains, respectively. The peak point P at the waveform in (a) is transformed to the peak point P^* at the waveform in (b).
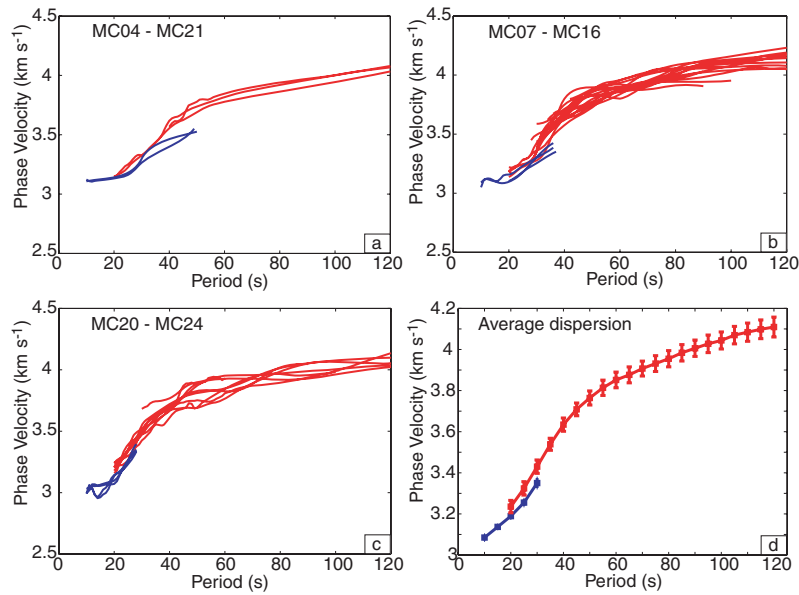
Figure 7. Rayleigh-wave phase velocity dispersion measurements from the EGF and TS analysis: (a–c) Rayleigh-wave phase velocity dispersion curves of different two-station paths from the EGF analysis for different months (blue lines) and from the TS analysis for different earthquakes (red lines); (d) average Rayleigh-wave phase velocity dispersion curve and the average standard errors for the studied area from the EGF analysis (blue line and error bars in the period bands 10–30 s) and from the TS method (red line and error bars in the period bands 20–120 s).

greatly enhances the efficiency and reliability of phase velocity measurements. Compared to the measurement of the group traveltime (i.e. the time of the (broad) peak at the envelope) that is needed to determine the group velocities (e.g. Shapiro & Campillo 2004; Sabra *et al.* 2005a), the measurement of the peak traveltime for the phase velocities appears to be more accurate.

We infer the Rayleigh-wave phase velocity dispersion (e.g. blue lines in Figs 7a, b and c) for $T = 10$–50 s from vertical component EGFs for all possible two-station paths for the 4 months considered. Recall that the maximum period for the phase velocity measurement of each station pair is set by eq. (6) and, thus, the distance between the pair of receivers considered. For each path we calculate the average phase velocity and its standard error at each period. Finally, we obtain the average phase velocities for the array area (with the corresponding standard errors) by averaging the phase velocity (and its standard error) for all paths (Fig. 7d). The standard errors are quite small (about 0.01 km s^{-1} at 10–20 s, 0.015 km s^{-1} at 25 s, and 0.024 km s^{-1} at 30 s), which shows that EGFs from one-bit cross-correlation of 1 month of ambient seismic noise can give precise phase velocity measurements at the relatively short periods considered here (i.e. 10–30 s). For the phase velocity maps presented in the next section we do not use EGF-derived phase velocity measurements at the periods larger than 30 s because at longer periods the EGFs are less robust, in part because the far-field approximation (6) and the lateral extent of the array limit the number of data at those periods.

4 PHASE VELOCITY MAPS

4.1 Phase velocity maps from EGFs

We use the technique by Tarantola & Valette (1982) and Tarantola & Nercessian (1984) to invert the phase velocity dispersion measurements from EGFs to obtain the Rayleigh-wave phase velocity variation at different periods. We first obtain the phase slowness (the inverse of the phase velocity) maps by minimization of the cost

function

$$\Phi(\mathbf{s}) = (\mathbf{t} - \mathbf{t}_{\text{obs}})^{\text{T}} \mathbf{C}_D^{-1} (\mathbf{t} - \mathbf{t}_{\text{obs}}) + (\mathbf{s} - \mathbf{s}_p)^{\text{T}} \mathbf{C}_M^{-1} (\mathbf{s} - \mathbf{s}_p); \qquad (7)$$

from this we calculate the phase velocity distribution. In eq. (7), $\mathbf{s}$ is the 2-D phase slowness model, $\mathbf{s}_p$ is the *prior* 2-D phase slowness model, $\mathbf{t}_{\text{obs}}$ is the vector of observed phase traveltimes (the ith component is given by $(\mathbf{t}_{\text{obs}})_i = \Delta_i / c_i$, i runs through all combinations AB, see eq. 5), $\mathbf{t}$ is the predicted phase traveltime from the phase slowness model $\mathbf{s}$, $\mathbf{C}_D$ is the data covariance matrix describing the data uncertainties, and $\mathbf{C}_M$ is the *prior* model covariance function.

The predicted phase traveltime for the ith path is determined by $t_i = \int_0^{\Delta_i} s \, d\Delta$, where the integral is along the great-circle path and Δ_i is the interstation distance. The region under study is parametrized by means of $0.5° \times 0.5°$ grid points. The phase slowness s at any point in the inversion area is determined from the values at four surrounded grid points using bilinear interpolation. The *prior* model covariance function $\mathbf{C}_M(r_1, r_2)$ represents the covariance between model estimates at r_1 and r_2:

$$\mathbf{C}_M(r_1, r_2) = \sigma_s^2 \exp\left(-\frac{(r_1 - r_2)^2}{2L^2}\right), \qquad (8)$$

where $\sigma_s = \sigma_c / c_0^2$ represents the *prior* slowness uncertainty, σ_c is the *prior* phase velocity uncertainty with respect to the homogenous starting model with phase slowness $1/c_0$, and L is the correlation length of the model. We set σ_c to 0.15 km s^{-1}, and c_0 is the average phase velocity (at a certain period) in the region. On the basis of results from resolution tests, we choose the correlation length L, which determines the smoothness of the phase slowness maps, to be 100 km.

In order to investigate whether the phase velocity measurements from different months influence the inversion results, we invert the phase velocities at $T = 10$ s of each of the 4 months under consideration to obtain the Rayleigh-wave phase velocity maps for the four separate months using a homogeneous starting model. The results (Fig. 8) are quite similar to one another, which confirms the stability of the EGFs with regard to temporal variations in regional
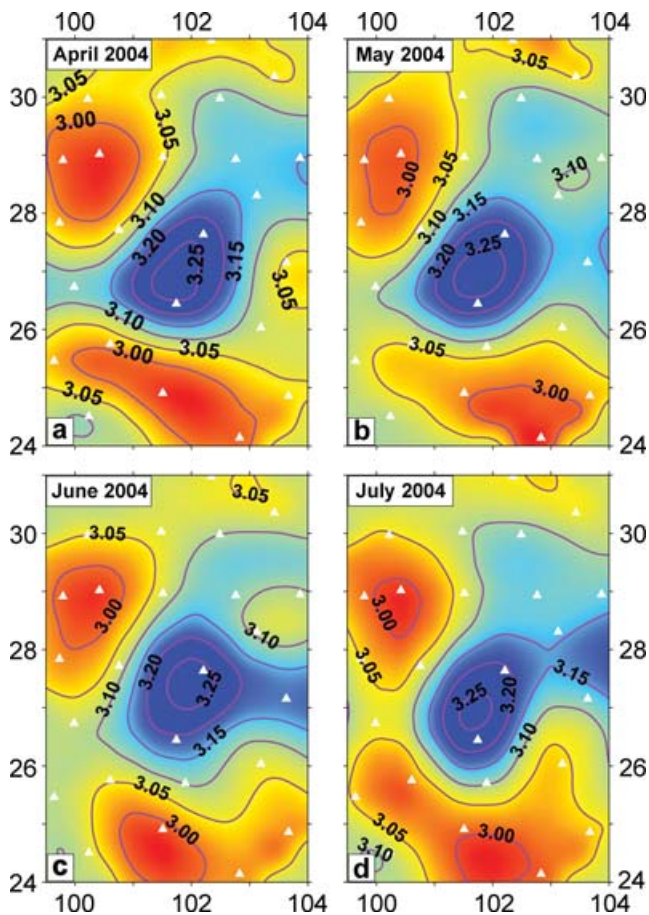
Figure 8. Comparison of inverted phase velocity maps at period $T = 10$ s for four different months from the EGF analysis. White triangles show station location. The contour values are Rayleigh-wave phase velocities (km s^{-1}). Red and blue represents lower and higher velocity, respectively.

(micro-)seismicity. Subsequently, we use the phase velocities for each path averaged over the 4 months to obtain the phase velocity maps at 10, 15, 20, 25 and 30 s. Figs 9(a)–(c) shows the path coverage for the averaged dispersion data at $T = 10$, 20, and 30 s. At 10 s the number of averaged phase velocity measurements is 267, which is close to the maximal number (300) of two-station measurements for a seismic array with 25 stations. A series of checkerboard resolution tests suggests that in much of the area under study the horizontal resolution of the phase velocity maps derived from the EGFs is $\sim$ 100 km (Fig. 10b). Figs 11(a)–(c) show examples of phase velocity maps at $T = 10$, 20, and 30 s.

We evaluated the reliability of the phase velocity measurements from EGFs by a comparison with group velocities. Ignoring the distortion of the amplitude spectrum, we use a frequency–time analysis to measure from EGFs the group velocities in the period band 10–30 s. Using $g = d\omega/dk = c + k \cdot dc/dk$, with c and g the phase and group velocities, respectively, we then predict c from the measured g. The average absolute discrepancy between c thus inferred and the phase velocities measured directly from EGFs gradually increases from $\sim$0.01 km s^{-1} at $T \sim 10$ s to $\sim$0.04 km s^{-1} at $T \sim 30$ s, which for our study region is about an order of magnitude smaller than the observed variation ($\sim$0.3–0.4 km s^{-1}, Figs 11(a)–(c)). Compared to the average phase velocities inferred directly from EGFs (Fig. 7d), the average phage velocities derived from the group velocities are 0.01–0.02 km s^{-1} higher in the period band 20–30 s, which may

indicate that at these periods the phase velocity measurements are slightly underestimated (by about $\sim$0.3–0.6 per cent). The discrepancy increase with increasing period, suggesting that phase velocity measurements at shorter periods (10–20 s) are more reliable than at relatively longer periods ($T > 20$ s), in accord with Fig. 7(d).

4.2 Phase velocity maps from two-station (TS) method

We use a TS method (Yao *et al.* 2005) to measure Rayleigh-wave fundamental-mode phase velocity dispersion in the period bands 20–120 s. We assume surface-wave propagation along a great-circle path between earthquake and station. For each two-station dispersion measurement, in order to suppress the influence of the structure between the earthquake and the station nearest to it, we require that the earthquake and the station pair considered are (approximately) on the same great circle path, with the maximum two deviation angles (α and β in Fig. 12a) each less than $3°$. The average phase velocity of the two-station path is then approximated by

$$c(T) \approx \frac{\Delta_2 - \Delta_1}{\Delta t(T)}, \qquad (9)$$

where $c(T)$ is the phase velocity at period T, $\Delta t(T)$ is the phase traveltime at period T estimated from cross-correlation of narrow band-pass filtered waveforms at central period T at the two stations,[1] Δ_2 is the distance from the earthquake to the farthest station, and Δ_1 is the distance to the nearest station. For a small difference in propagation distance, a small error δt in the measurement of $\Delta t(T)$ will cause a considerable error in the phase velocity measurements, in particular at longer periods. For example, if $\Delta_2 - \Delta_1 = 200$ km, $\Delta t = 60$ s at $T = 20$ s (i.e. $c \sim$3.33 km s^{-1}), $\Delta t = 48$ s at $T = 100$ s (i.e. $c \sim$4.17 km s^{-1}), and $\delta t = 1$ s, the relatively error in the phase velocity measurement $\delta c/c = \delta t/\Delta t$ is $\sim$1.7 per cent at $T = 20$ s and $\sim$2.1 per cent at $T = 100$ s. In order to make reliable measurements at relatively longer periods, we require $\Delta_2 - \Delta_1$ to be at least half of the wavelength ($\lambda = c(T) \cdot T$); here we refer to this as the half-wavelength criterion. Consequently, the available phase velocity measurements decrease as the period increases (Figs 9d–j), which yields a relatively high path density at the shorter periods and lower path density at the longer periods. Note that this has an effect similar to the effect of the far-field approximation described above.

In this way, we obtain about 600 phase velocity dispersion curves for $T = 20$–120 s from about 160 earthquakes with $5.0 \le M_w \le 7.0$ and depth <100 km from 2003 October to 2004 September (Fig. 13). Fig. 14 shows an example of phase velocity measurements using the image transformation technique. Red lines in Figs 7(a)–(c) show the extracted dispersion curves for three two-station paths from different earthquakes. Phase velocity dispersion measurements for the same two-station path are averaged to make 158 average dispersion curves within the period bands 20–120 s, and the standard errors of the phase velocities are calculated for paths with at least two measurements. The average phase velocities (red line in Fig. 7d) and the corresponding standard errors (red error bars in Fig. 7d) for $T = 20$–120 s are then obtained by averaging all the phase velocity measurements and the standard errors for each period. The standard error increases with increasing period mainly

---

[1]We note that, formally speaking, the measurement yielded by time domain cross-correlation is not the traveltime proper and should be interpreted with the appropriate finite frequency sensitivity kernel (see, e.g. Dahlen *et al.* 2000; De Hoop & Van der Hilst 2005).
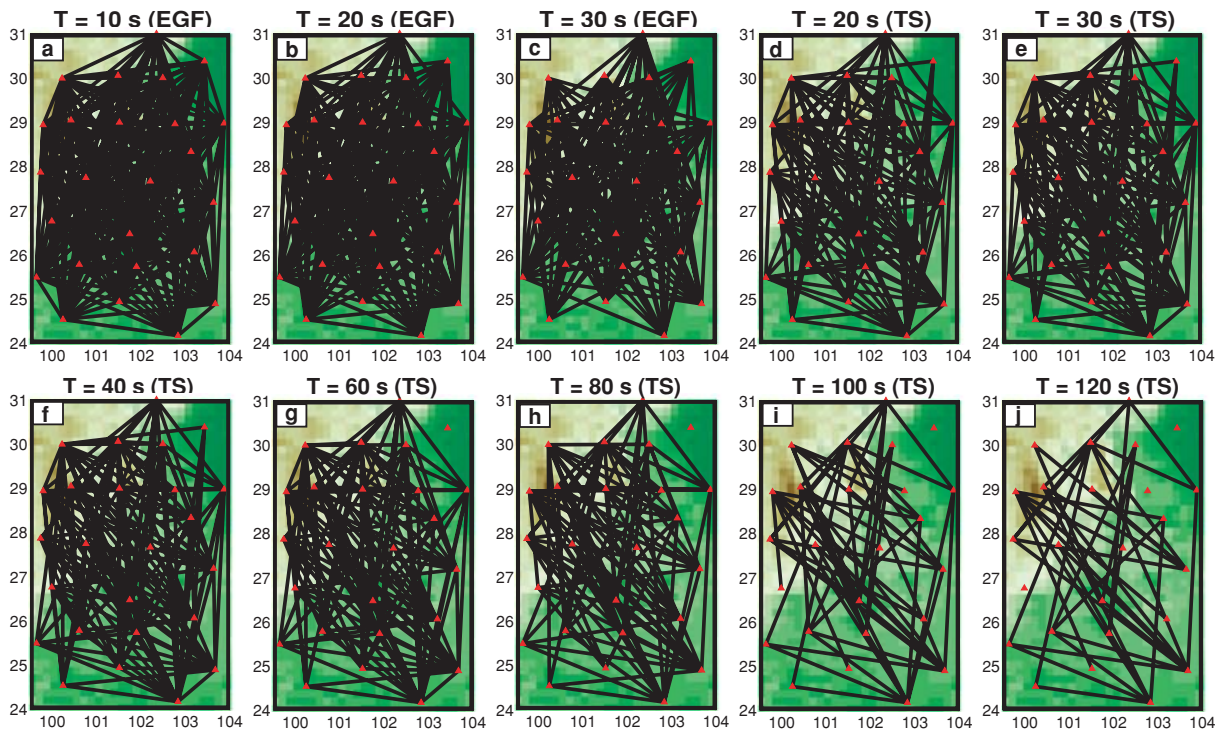
Figure 9. Path coverage of Rayleigh-wave phase velocity measurements at different periods: (a–c) for the EGF analysis using the average phase velocity dispersion data over 4 months for each path; (d–j) for the TS method using the average phase velocity dispersion data over different earthquakes for each path. Red triangles show the location of stations. This figure demonstrates that the path coverage is densest where it is needed most, namely, at short periods, whereas the coverage for lower frequency data (which constrain the longer wavelength structures) is much sparser.

due to the decrease of the interstation phase traveltime $\Delta t(T)$. At the short and intermediate periods (20–80 s), the standard error is about 0.03–0.04 km s^{-1}. However, the standard error increases to ∼0.05 km s^{-1} at 120 s. The standard error given here are lower estimates because we do not consider errors from other sources, for example, scattering, off-great-circle propagation, etc.

The path coverage of the average phase velocity measurements at different periods, shown in Figs 9(d)–(j), is quite good at periods 20–80 s but only about 40 measurements could be made at longer periods (100–120 s) due, in part, to the half wavelength criteria and, in part, to the relatively poor data quality at these long periods. We use the same inversion scheme as described in Section 4 to produce phase velocity maps for $T = 20$–120 s, except that we set the correlation length L to 100 km at 20–60 s, to 150 km at 65–80 s, and to 200 km at 85–120 s in view of the fact that the physical resolution is limited by the predominant wavelengths considered. The phase velocity maps at 20, 30, 40, 60, 80, 100 and 120 s are shown in Figs 11(d)–(j). The lateral resolution of these maps is about 100–200 km at 20–60 s (Figs 10c and e) and 200–300 km at 65–120 s (Fig. 10f).

4.3 Wave speed variations beneath SE Tibet and SW China

In a separate study (Yao *et al.* 2006) the phase velocity maps will be inverted for 3-D shear wave velocity structure of the crust and upper mantle. Here we merely make some first order observations. In the entire frequency band considered here, high phase velocities mark the (north)eastern part of the array area, close to the Sichuan Basin. In contrast, phase velocity maps at short and intermediate pe-

riods ($T = 10$–80 s), shown in Figs 11(a)–(h), exhibit a pronounced low-velocity structure in the northwestern part of the array area (SE Tibet), which suggests a low shear wave velocity structure in the crust and upper mantle. At $T = 100$–120 s this low-velocity anomaly is mapped further South (Figs 11i and j). These results are—at least qualitatively—consistent with the finding from traveltime that P-wave propagation is anomalously slow in the upper mantle beneath SE Tibet and the Red River area (Li *et al.* 2006), which may be of relevance for geodynamical models of lower or middle crustal flow as suggested by Royden *et al.* (1997) and Beaumont *et al.* (2004).

5 DISCUSSION: COMPARISON OF THE EGF AND TS RESULTS

Phase velocity dispersion measurements were obtained from the EGF and TS analysis in different period bands. The phase velocities at the relatively short period bands (20–30 s) are similar for both methods (Figs 7a, b and c), but the discrepancies become larger (>2 per cent) at periods larger than 30 s (e.g. Fig. 7a). The average phase velocities from the EGF analysis are 0.046 km s^{-1}, 0.069 km s^{-1}, 0.080 km s^{-1} lower than the results from the TS method at 20, 25, and 30 s, respectively. Note that these differences exceed the uncertainties for either method which suggests that the discrepancy may be systematic. Comparison of the phase velocity maps at 20 s (Figs 11b and d) and 30 s (Figs 11c and e) shows that the overall low- and high-velocity features are quite similar but that the TS method gives phase velocities that are about 1–3 per cent higher than the EGF results.

Several factors can contribute to this discrepancy. For the EGF analysis, in addition to the possibility of (slightly) underestimating
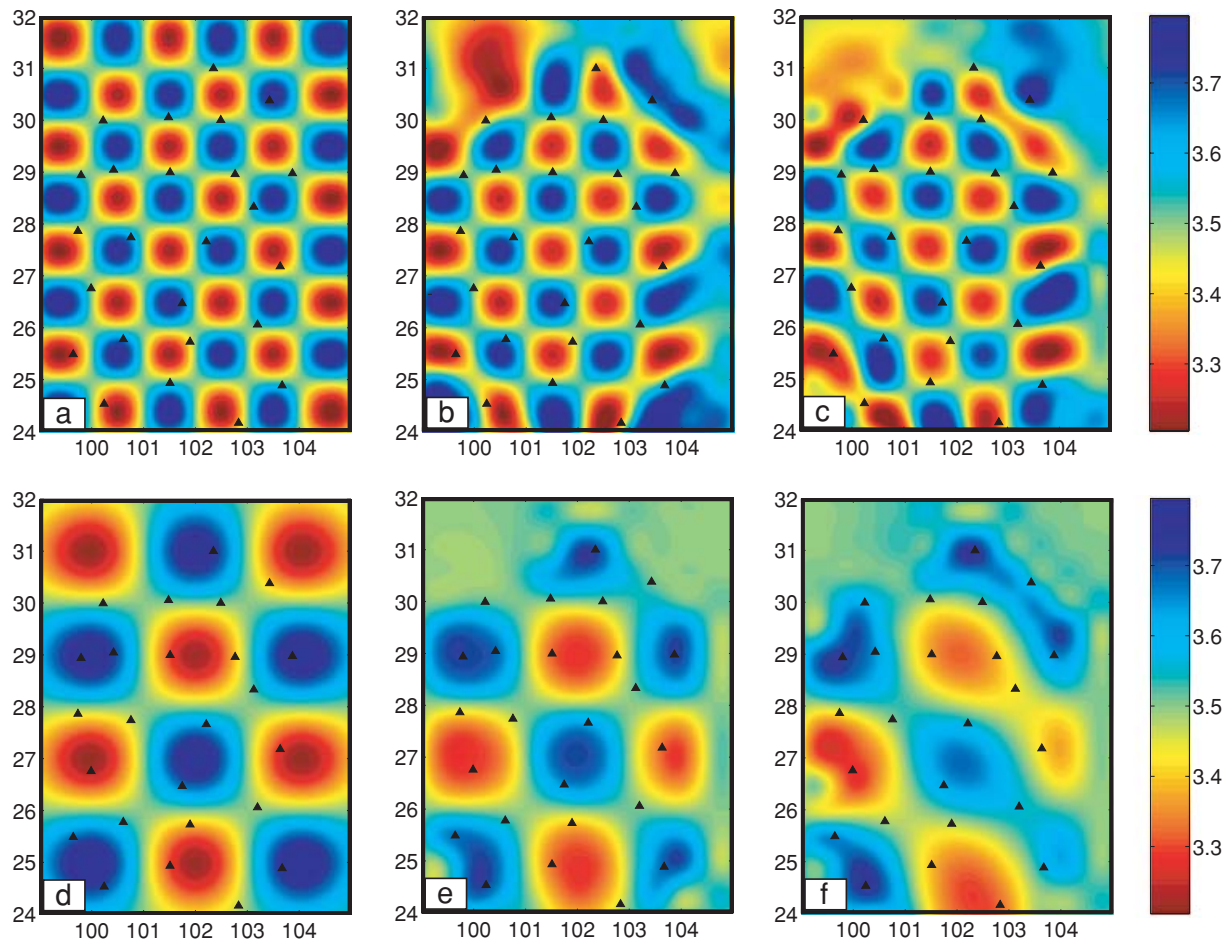
Figure 10. Resolution tests: (a) input $1° \times 1°$ model; (b) recovery of $1° \times 1°$ model for the path coverage at $T = 10$ s (EGF) shown as Fig. 9(a); (c) recovery of $1° \times 1°$ model for the path coverage at $T = 40$ s (TS) shown as Fig. 9(f); (d) input $2° \times 2°$ model; (e) recovery of $2° \times 2°$ model for the path coverage at $T = 60$ s (TS) shown as Fig. 9(g); (f) recovery of $2° \times 2°$ model for the path coverage at $T = 80$ s (TS) shown as Fig. 9(h). Black triangles show the location of stations. The values of the colour bar are Rayleigh-wave phase velocities (km s^{-1}).

the phase velocity measurements (see remarks at the end of Section 4.1), the error in the estimation of interstation phase velocities mainly comes from: (1) incomplete recovery of the Green's function due to the inhomogeneous distribution of the noise sources; and (2) off-great-circle propagation due to interstation velocity anomalies. The first effect is hard to quantify, but the observed stability of the EGFs between 10–30 s suggests that it is relatively small. The second will underestimate interstation phase velocities because the length of off-great-circle paths is always larger than that of great-circle paths (Fig. 12b).

For the TS method there are other sources of inaccuracy. The incoming surface waves are approximated as plane waves. If surface waves propagate along the great-circle path (solid parallel lines with arrow in Fig. 12c), the interstation phase velocity (c_{gc}) is estimated by $c_{gc} \approx (\Delta_2 - \Delta_1)/\Delta t \approx d_{A'B}/\Delta t$, where Δ_1, Δ_2, and Δt are the same as those defined in eq. (9), and $d_{A'B}$, the difference in great-circle propagation distance between two stations, is the distance of the solid line $A'B$ in Fig. 12(c). When the incoming surface wave (dashed parallel lines with arrow in Fig. 12c) deviates from the great-circle propagation path with angle θ (defined in Fig. 12c), the interstation phase velocity of this off-great-circle propagation (c_{ogc}) is estimated by $c_{ogc} \approx d_{A''B}/\Delta t$, where $d_{A''B}$, the difference in off-great-circle propagation distance between two stations, is the

distance of the dashed line $A''B$ in Fig. 12(c). Therefore, the ratio $c_{ogc}/c_{gc} = d_{A''B}/d_{A'B} = \cos(\beta + \theta)/\cos \beta$, where β is the deviation angle in Fig. 12(c) which is same as that in Fig. 12(a). For a very small angle (in our study $\beta \leq 3°$), the ratio c_{ogc}/c_{gc} is less than 1 almost for all θ except in a very small range $-2\beta \leq \theta \leq 0°$ (Fig. 15), which indicates that the interstation phase velocity measurements based on the approximation of great-circle propagation will commonly give a higher estimation (e.g. if $\beta = 0°$, the phase velocity is $\sim$1.5 per cent higher estimated when $\theta = 10°$ as shown in Fig. 15).

Other reasons for the frequency-dependent discrepancy of phase velocities between the two methods include the fact that the surface-wave sensitivity zone in the TS method is much larger than the zone of sensitivity to structure in the case of the EGF analysis as shown in Fig. 12(d), especially at longer periods (Yoshizawa & Kennett 2002; Spetzler *et al.* 2002; Zhou *et al.* 2004). In contrast, the measurements from the EGF analysis are only sensitive to heterogeneity in a very narrow zone between the two stations (Fig. 12d), which provides a much higher resolution of the structure along the two-station path. Most earthquakes used for the TS analysis are located to the southeastern direction of the array (Fig. 13); the broader sensitivity kernel for the TS method mainly samples areas with relatively high velocities (e.g. Sichuan basin), whereas wave speeds under the array are mainly slow. This would result in a higher estimation of phase
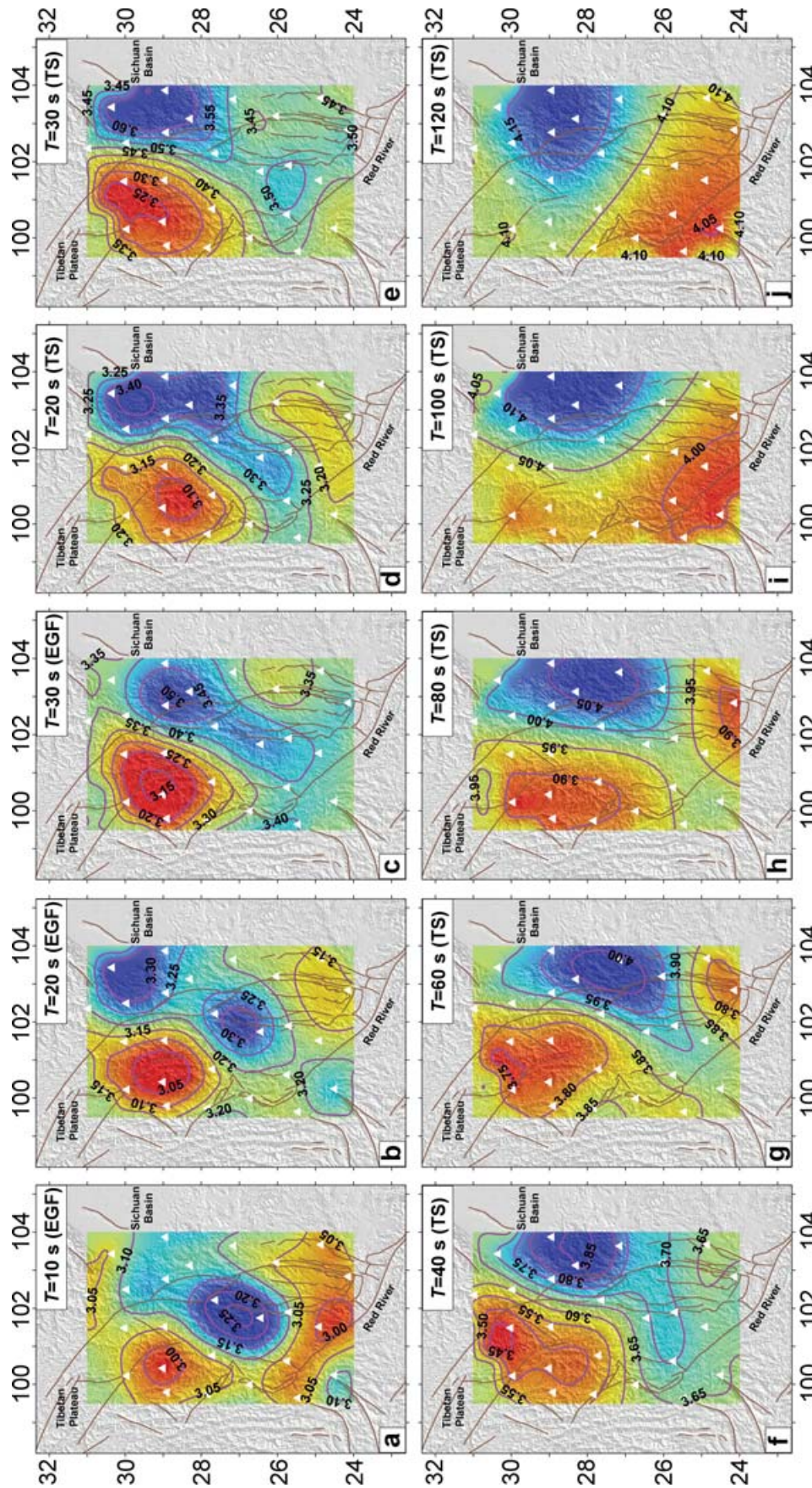
Figure 11. Rayleigh-wave phase velocity maps at different periods (10–120 s): (a–c) are the inversion results (10–30 s) from the EGF analysis using the average phase velocity dispersion data over 4 months for each path; (d–j) are the inversion results (20–120 s) from the TS method. Black triangles show station locations. The corresponding path coverage maps are shown in Fig. 9. The contour values are Rayleigh-wave phase velocities (km s⁻¹). Red and blue represents lower and higher velocity, respectively. Brown lines depict the major faults in the studied area.
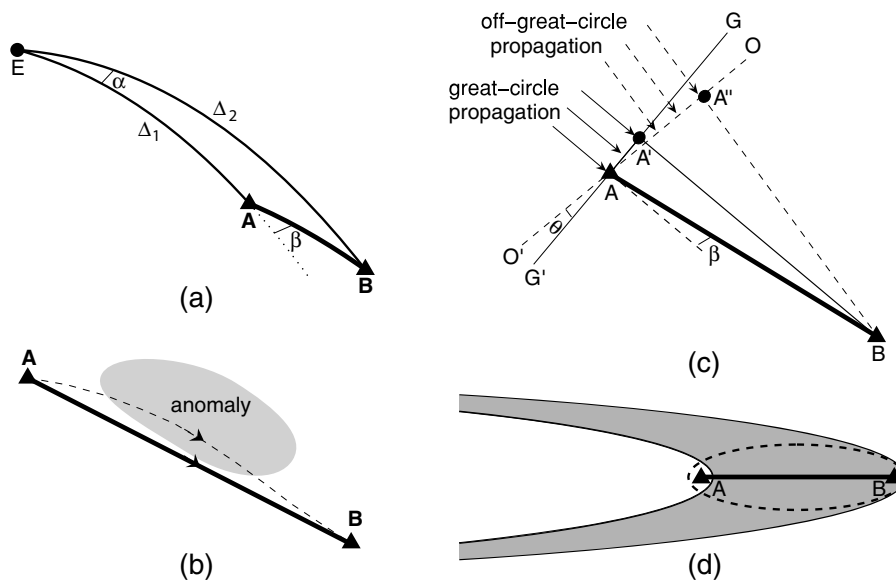
Figure 12. (a) Illustration of two deviation angles α and β defined in the TS method: α is the azimuthal difference of the earthquake (E) to the two stations (A and B, with A nearest to the earthquake); β is the azimuthal difference between the earthquake (E) to the station A and the station A to the station B. The solid lines are all great-circle paths and the dashed line is the extended great-circle path from E to A. Δ_1 is the great-circle distance between E and A and Δ_2 is the great-circle distance between E and B. (b) Illustration of off-great-circle propagation of surface waves between source A and receiver B for the EGF analysis. The solid line represents the path of great-circle propagation between two stations A and B; the dashed line is the path of off-great-circle propagation due to the influence of the velocity anomaly region (shaded area). The distance of off-great-circle path (dashed line) is always larger than that of the great-circle path (solid line), which results in a lower estimation of the average phase velocity between two stations because the estimated phase traveltime from the EGF is the same. (c) Illustration of great-circle propagation (solid parallel lines with arrow) and off-great-circle propagation (dashed parallel lines with arrow) of surface waves for the array TS analysis, where the solid triangles A and B are the two stations, the solid line GG' is the wave front of great-circle propagating surface waves and is perpendicular to the solid line $A'B$ with distance (approximately) equal to $\Delta_2 - \Delta_1$ in (a), the dashed line OO' is the wave front of off-great-circle propagating surface waves and is perpendicular to the dashed line $A''B$, the deviation angle β is the same as that defined in (a), and the off-great-circle angle θ is defined as the angle from GG' to OO' (clockwise is defined to be positive here). (d) Illustration of surface-wave sensitivity zones for the EGF analysis and the TS method. The shaded area is the sensitivity zone for the TS method, which is much broader than the sensitivity zone (the area inside the dashed ellipse) for the EGF analysis. The solid triangles A and B are the two stations. The solid line is the great circle path between the two stations.
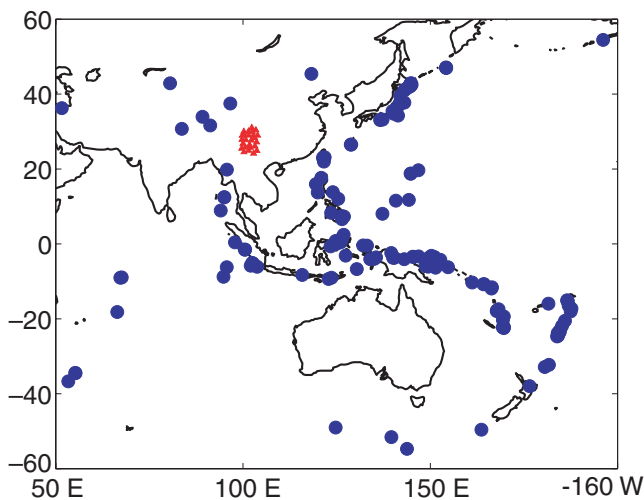

Figure 13. The location of earthquakes (blue solid circles) used in the TS method. The red solid triangles show the location of array stations.

velocities from the TS method than from EGF analysis. (NB this effect is likely to be small for low-frequency waves that are primarily sensitive to upper mantle structure.)

In combination, such physical, geometrical, and structural factors explain why, for our study region, the interstation phase ve-

locity measurement from the TS method tends to be higher than that from the EGF analysis because the latter tends to underestimate the average phase velocities while at short period the former may overestimate them.

The EGF analysis can provide more reliable phase velocity measurements at relatively short periods (10–30 s, in this study), but for array tomography studies it becomes less accurate at longer periods because of the use of the far-field approximation. Furthermore, our analysis shows that, for our array, the dispersion measurements become unstable at periods larger than 30 s. In contrast, the TS method can be used to measure phase velocities to much longer periods (e.g. to about 100 s for a two-station path with distance 200 km with the TS method, compared to only ∼20 s with the EGF analysis). However, the phase velocity measurements at 20–30 s from the TS method are less reliable mainly due to the effects of strong scattering on the shorter period part ($T < 30$ s) of the waveform, off-great-circle propagation and much broader sensitivity zone. To exploit the strengths of both methods, we combine the dispersion data from the EGF and TS analysis to construct phase velocity maps in the period bands from 10–120 s, which (in a separate study) we will invert for 3-D shear wave velocity structure of the crust and upper mantle.

6 SUMMARY

We have determined EGFs from the cross-correlation of either (monthly) ambient seismic noise or surface-wave coda recorded at
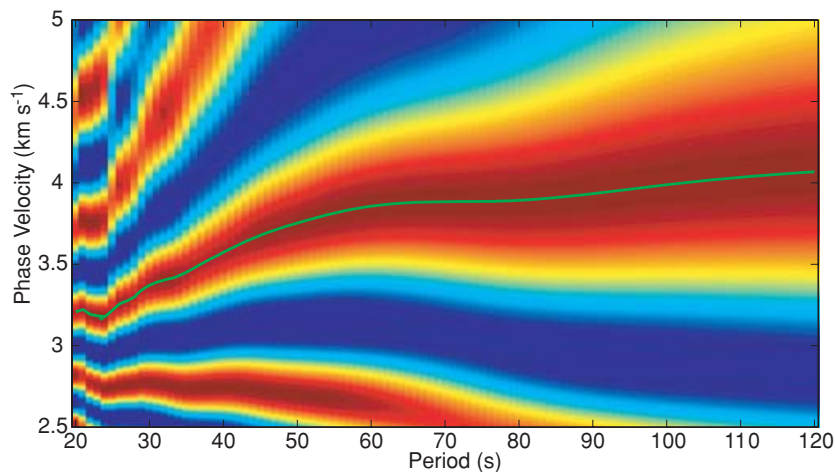
Figure 14. Example of extracted dispersion curve (green curve on the $c - T$ image) for the station pair MC20–MC05 using the TS method based on the image transformation technique. The earthquake locates at $(-5.8010°, 102.0280°)$ with $M_w = 5.5$, depth $= 10.0$, and source time $= 2003/12/24$, 11:33:04.36.
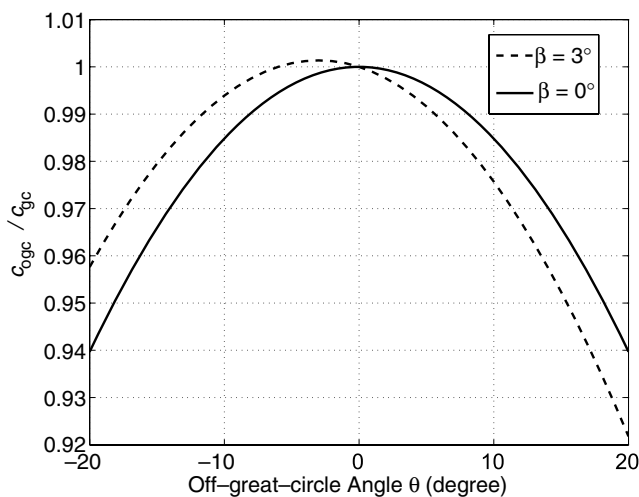

Figure 15. The ratio of the interstation phase velocity estimated from off-great-circle propagation (c_{ogc}) to the interstation phase velocity estimated from great-circle propagation (c_{gc}) at given off-great-circle angle θ with the deviation angle $\beta = 0°$ (solid curve) and $\beta = 3°$ (dashed curve) as illustrated in Fig. 12(d).

the MIT-CIGMR broad-band network (25 stations) on the southeastern Tibetan plateau in Sichuan and Yunnan provinces, SW China. We used an image transformation technique and a far-field approximation of the surface-wave Green's function to make accurate phase velocity dispersion measurements for relatively short period data ($T = 10$–30 s) for all possible two-station combinations in the array. We showed that noise correlations for different months give consistent results, that the EGFs are not biased by individual earthquakes, and that the results from ambient noise or surface-wave coda are very similar. However, the EGFs are time asymmetric (one sided) for stations aligned in the N–S direction, which we attribute to the paucity of seismicity north of the array. For longer periods we have measured interstation phase velocities using classical TS analysis, and the combination of these methods provides dispersion curves and phase velocity maps over a very broad period range ($T = 10$–120 s), which can be used for high-resolution tomographic studies of the crust and upper mantle beneath this region.

Application of a far-field approximation (in the case of the EFG analysis) or a half-wavelength criterion (for the TS analysis) produces a situation that is attractive for multiscale surface-wave tomography: the density of path coverage is proportional to the periods under consideration decreases. Tests with synthetic data demonstrate that our array data should be able to resolve heterogeneity on length scales comparable to and larger than the interstation spacing (~ 100 km and up, for our array). In future studies this will be exploited in multiresolution tomography for isotropic and (azimuthally) anisotropic variations in shear wave speed in the crust and upper mantle beneath SE Tibet.

Phase velocities at short and intermediate periods ($T = 10$–80 s) are prominently low in SE Tibet, suggesting that shear wave propagation may be slow in the shallow part of the lithosphere in SE Tibet. Moreover, phase velocities in the entire period band considered here ($T = 10$–120 s) are high in the vicinity of the Archean Sichuan craton.

ACKNOWLEDGMENTS

REFERENCES

Beaumont, C., Jamieson, R.A., Nguyen, M.H. & Medvedev, S., 2004. Crustal channel flows: 1. Numerical models with applications to the tectonics of the Himalayan-Tibetan orogen, *J. geophys. Res.,* **109,** B06406, doi:10.1029/2003JB002809.

Brisbourne, A. & Stuart, G., 1998. Shear-wave velocity structure beneath North Island, New Zealand, from Rayleigh-wave interstation phase velocities, *Geophys. J. Int.,* **133,** 175–184.

Campillo, M. & Paul, A., 2003. Long-Range correlations in the diffuse seismic coda, *Science,* **299,** 547–549.

Dahlen, F.A. & Tromp, J., 1998. *Theoretical Global Seismology*, Princeton Univ. Press, Princeton, New Jersey.

Dahlen, F., Hung, S.-H. & Nolet, G., 2000. Fréchet kernels for finite-frequency traveltimes—I. Theory, *Geophys. J. Int.,* **141,** 157–174.

De Hoop, M.V. & Van der Hilst, R.D., 2005. On sensitivity kernels for 'wave-equation' transmission tomography, *Geophys. J. Int.,* **160,** 621–633.

Engdahl, E.R., Van der Hilst, R.D. & Buland, R.P., 1998. Global teleseismic earthquake relocation from improved travel times and procedures for depth determination, *Bull. seism. Soc. Am.,* **88,** 722–743.

Huang, Z., Su, W., Peng, Y., Zheng, Y. & Li, H., 2003. Rayleigh wave tomography of China and adjacent regions, *J. geophys. Res.,* **108**(B2), 2073, doi:10.1029/2001JB001696.

Knopoff, L., Muller, S. & Pilant, W.L., 1966. Structure of the crust and upper mantle in the Alps from the phase velocity of Rayleigh waves, *Bull. seism. Soc. Am.,* **56,** 1009–1044.

Li, C., Van der Hilst, R.D. & Toksoz, M.N., 2006. Constraining P-wave velocity variations in upper mantle beneath Southeast Aisa, *Phys. Earth planet. Inter.,* **154,** 180–195.

Lobkis, O.I. & Weaver, R.L., 2001. On the emergence of the Green's function in the correlations of a diffusive field, *J. acoust. Soc. Am.,* **110,** 3011–3017.

Passier, M.L., Van der Hilst, R.D. & Snieder, R.K., 1997. Surface wave wave-form inversions for local shear-wave velocities under eastern Australia, *Geophys. Res. Lett.,* **24,** 1291–1294.

Paul, A., Campillo, M., Margerin, L., Larose, E. & Derode, A., 2005. Empirical synthesis of time-asymmetrical Green functions from the correlation of coda waves, *J. geophys. Res.,* **110,** B08302, doi:10.1029/2004JB003521.

Roux, P., Sabra, K.G., Kuperman, W.A. & Roux, A., 2005. Ambient noise cross correlation in free space: theoretical approach, 2005, *J. acoust. Soc. Am.,* **117,** 79–84.

Royden, L.H., Burchfiel, B.C., King, R.W., Wang, E., Chen, Z., Shen, F. & Yuping, L., 1997. Surface deformation and lower crustal flow in eastern Tibet, *Science,* **276,** 788–790.

Sabra, K.G., Gerstoft, P., Roux, P., Kuperman, W.A. & Fehler, M.C., 2005a. Extracting time-domain Greens function estimates from ambient seismic noise, *Geophys. Res. Lett.,* **32,** L03310, doi:10.1029/2004GL021862.

Sabra, K.G., Gerstoft, P., Roux, P. & Kuperman, W.A., 2005b. Surface wave tomography from microseisms in Southern California, *Geophys. Res. Lett.,* **32,** L14311, doi:10.1029/2005GL023155.

Shapiro, N.M. & Ritzwoller, M.H., 2002. Monte-Carlo inversion for a global shear-velocity model of the crust and upper mantle, *Geophys. J. Int.,* **151,** 88–105.

Shapiro, N.M. & Campillo, M., 2004. Emergence of broadband Rayleigh waves from correlations of the ambient seismic noise, *Geophys. Res. Lett,* **31,** L07614, doi:10.1029/2004GL019491.

Shapiro, N.M., Campillo, M., Stehly, L. & Ritzwoller, M.H., 2005. High-resolution surface wave tomography from ambient seismic noise, *Science,* **307,** 1615–1618.

Simons, F.J., van der Hilst, R.D., Montagner, J.P. & Zielhuis, A., 2002. Multimode Rayleigh wave inversion for heterogeneity and azimuthal anisotropy of the Australian upper mantle, *Geophys. J. Int.,* **151,** 738–754.

Spetzler, J., Trampert, J. & Snieder, R., 2002. The effect of scattering in surface wave tomography, *Geophys. J. Int.,* **149,** 755–767.

Tarantola, A. & Nercessian, A., 1984. Three-dimensional inversion with blocks, *Geophys. J. R. astr. Soc.,* **76,** 299–306.

Tarantola, A. & Valette, B., 1982. Generalized nonlinear inverse problem solved using the least squares criterion, *Rev. Geophys. Space Phys.,* **20**(2), 219–232.

Trampert, J. & Woodhouse, J., 1996. High resolution global phase velocity distributions, *Geophys. Res. Lett.,* **23,** 21–24.

Weaver, R.L. & Lobkis, O.I., 2004. Diffuse fields in open systems and the emergence of the Green's function. *J. acoust. Soc. Am.,* **116,** 2731–2734.

Yao, H., Xu, G., Zhu, L. & Xiao, X., 2005. Mantle structure from inter-station Rayleigh wave dispersion and its tectonic implication in western China and neighboring regions, *Phys. Earth planet. Inter.,* **148,** 39–54.

Yoshizawa, K. & Kennett, B.L.N., 2002. Determination of the influence zone for surface wave paths, *Geophys. J. Int.,* **149,** 441–454.

Zielhuis, A. & Nolet, G., 1994. Deep seismic expression of an ancient plate boundary in Europe, *Science,* **265,** 79–81.

Zhou, Y., Dahlen, F.A. & Nolet, G., 2004. Three-dimensional sensitivity kernels for surface wave observables, *Geophys. J. Int.,* **158,** 142–168.